Advancing 60-GHz SISO Radar: Additively Manufactured Leaky Wave Antenna With Enhanced Beam Steering

Jasmin Gabsteiger, *Student Member, IEEE*, Christian Robisch, Alexander Koelpin, *Fellow, IEEE*, and Fabian Lurz, *Senior Member, IEEE*

***Abstract*—In this work, a waveguide-based leaky wave antenna (LWA) for beam scanning operation at 60 GHz is presented, fabricated, and experimentally investigated. It employs a slotted radiator in a rectangular waveguide, achieves a beam squint of 76° with 5.5-GHz bandwidth, offering enhanced angular resolution. The antenna employs dual feeding, thereby virtually doubling the bandwidth, which permits more beam scan angle per employed physical bandwidth in radar systems for precise angle estimation. The antenna was fabricated using SLA 3-D printing and subsequently silver-coated, enabling efficient production of complex 3-D antenna geometries. As expected, printing inaccuracies and metallization processes influence the antenna gain and beam squint. However, these effects can not only be reduced but even fully eliminated through targeted optimization of the manufacturing process, as demonstrated in this article. By combining application-specific antenna design with optimized fabrication techniques, best-in-class performance can be achieved despite the constraints of additive manufacturing. Compared with previous works, the antenna presented herein offers a unique combination of a large squint angle, high-operating frequency, and practical manufacturability. By combining the beam squint with dual feeding, a balance between high-range resolution and precise angle estimation is achieved in radar applications.**

***Index Terms*—Additive manufacturing, angle estimation, leaky wave antenna (LWA), single input single output (SISO) radar.**

I. Introduction

FOR radar systems with limited resources, particularly those with few receive channels, enhancing the angular resolution poses a central challenge. Typically, the angular separation is highly dependent on the number of receiving channels, which does not provide an optimal solution for resource-constrained systems [1]. An ideal approach should therefore enable precise angular resolution without demaning a large number of receive channels or a complex external control [2]. Current research offers various strategies to improve angular resolution. A conventional delay-and-sum beamformer processes the received signals by summing them with appropriate time delays to create a directional reception pattern. In contrast, classical multiple input–multiple output (MIMO) angle estimation using the fast Fourier transformation (FFT) applies a Fourier transform to the received data, thereby determining the angular spectrum [1]. Another common approach is the use of frequency-division multiple access (FDMA) in MIMO radar systems, where multiple transmitters operate simultaneously through range-division multiple-access (RDMA) and Doppler-division multiple-access (DDMA) [3]. In the RDMA method, each transmit element is assigned a small-frequency offset, which shifts the beat frequencies in the received signal and allows targets at similar ranges to be better distinguished. However, this also reduces the unambiguous range as the number of antennas increases, which is problematic for applications requiring high-range resolution. DDMA employs frequency offsets to shift signals in the Doppler dimension, thereby facilitating the discrimination of targets with different relative velocities. However, this comes at the expense of a reduced unambiguous velocity. While both techniques enhance target separation in their respective domains, the angular resolution remains dependent on the number of transmit and receiving channels. Furthermore, their implementation requires the precise frequency control and calibration of each channel, thereby increasing the hardware complexity. Another approach involves frequency-diverse arrays (FDAs), where each antenna element transmits with a minimal frequency deviation [4]. The resulting phase differences produce radiation patterns that vary with both angle and range. A specialized variant of this concept is the wavelength-array (WA), which, by optimizing the spacing between antenna elements, generates more stable and uniform radiation patterns. Although FDA-based systems offer additional degrees of freedom in target separation, they are not ideal for a resource-limited 60-GHz system with few antennas. The extremely fine frequency differences necessitate highly precise frequency synthesis and elaborate calibrations to avoid signal distortions especially considering the need for as many coherent synthesizers as there are channels. In addition, the external control is required to produce the desired beam shape, further complicating the system design. Another concept combines radar and communication systems through frequency-hopping (FH) waveforms [5]. In this approach, an MIMO radar transmission is implemented with FH signals, in which PSK symbols for information transfer are embed-

Received 23 June 2025; revised 19 March 2026; accepted 30 March 2026. Date of publication 23 April 2026; date of current version 9 July 2026. This work was supported by the Bavarian Ministry of Economic Affairs, Regional Development and Energy, Munich, Germany, through the Collaborative Project Embedded Machine Learning, under Grant DIK0349/02.
(Corresponding author: Jasmin Gabsteiger.)

Jasmin Gabsteiger and Fabian Lurz are with the Chair of Integrated Electronic Systems, Otto von Guericke University Magdeburg, 39106 Magdeburg, Germany (e-mail: jasmin.gabsteiger@fau.de).

Christian Robisch is with the Institute for Smart Electronics and Systems, Friedrich-Alexander Universitat Erlangen-Nuernberg, 91054 Erlangen, Germany.

Alexander Koelpin is with the Institute of High-Frequency Technology Hamburg, University of Technology Hamburg, 21073 Hamburg, Germany.
Digital Object Identifier 10.1109/TAP.2026.3681348

© 2026 The Authors. This work is licensed under a Creative Commons Attribution 4.0 License.
For more information, see https://creativecommons.org/licenses/by/4.0/

ded within each FH segment. This enables efficient use of radar resources without compromising the radar's primary function. However, the focus of this method is not on specifically enhancing angular resolution but rather on integrating additional communication capabilities. Although the MIMO functionality facilitates angular separation through multiple antenna elements, it requires precise synchronization between the communication symbols and the radar waveforms. For a system with few antennas that aims to achieve high angular resolution solely through the transmit signal without external control, this approach is not directly applicable. To address these challenges, a novel 3-D-printed approach and its special manufacturing-related design implications is presented in this publication, enabling the precise angular resolution without relying on a large number of individual receive channels or complex external control. The proposed concept is highly sensitive to small variations in the fabrication process, which can lead to significant performance deviations, particularly in terms of gain and beam squint. Therefore, the extensive process optimization is crucial. This work presents a carefully tuned and experimentally validated fabrication strategy that yields robust and reproducible performance, even under the constraints of additive manufacturing.

II. Concept of Radar Systems Utilizing Frequency-Steered Antenna Scanning Techniques

Leaky wave antennas (LWAs) are a special type of antenna that guides electromagnetic waves along a conductive structure while continuously radiating energy. The radiation angle of their main lobe directly depends on the operating frequency, as the phase constant of the wave along the structure changes with frequency. If a conventional frequency-modulated continuous wave (FMCW) radar system is combined with such an LWA, it enables the simultaneous determination of both the range and directional information of a target. By performing an analysis in the combined time and frequency domains, both the distance and the angle of an object can be accurately determined without the need for multiple channels or mechanical antenna scanning. With continuous frequency modulation, the primary beam direction varies according to the swept instantaneous frequency segment. Similar to conventional FMCW techniques, the signal reflected from the target is mixed with the transmitted waveform, resulting in a beat frequency that is directly proportional to the distance traveled. Simultaneously, this FMCW frequency ramp will lead to a frequency-dependent squint of the main lobe of the LWA. Since the antenna beam squint covers only a limited angular range for each frequency segment, the magnitude of the echo is variably modulated depending on the objects present within the respective solid angle. This frequency-dependent amplitude variation due to the beam scanning is preserved in the beat frequency spectrum and can be analyzed to determine the exact target direction given the designed dependency between instantaneous frequency and main lobe angle. Fig. 1 illustrates this principle: the upper left area and the graph below show the progression of the transmitted frequency spectrum, while the lower plot presents the power levels of the individual echoes, each distinctly marked. The sum of these signals, shown in black, represents the total received power. On the right side of Fig. 1, a scenario with two objects is depicted, with different antenna main lobes observable in various frequency segments. Here, a simple scenario with two targets and no multipath reflections is intentionally chosen to highlight the basic principles. In the first specific frequency interval, the first beam sector produces a strong echo, whereas an intervening frequency band that does not cover a relevant angle yields only a weak signal. At the end of the FMCW modulation cycle, the received power increases once again as a second target is illuminated in the corresponding frequency range, i.e., the corresponding main lobe angle.

A. Distance Measurement

The range resolution of an FMCW radar, defined as the minimum distance ΔR at which two scatterers can still be distinguished as separate targets, is given by

$$\Delta R = \frac{c}{2B} \tag{1}$$

where c denotes the speed of light and B represents the total bandwidth of the modulated signal. However, when an LWA with a squinting beam is employed, the entire frequency range is not continuously available for range resolution, as the target is illuminated only during a short-time window. Thus, only the bandwidth interval B' during the solid angle span of target illumination is usable. Assuming an almost constant antenna characteristic independent of the respective squint angle, particularly regarding the main lobe half-power beamwidth (HPBW) (defined by the 3-dB point) and the ratio of the scanning speed to the frequency difference, the degradation in range resolution can be quantified. The effective range resolution ΔR is reduced by a factor expressed as the quotient of the overall scanning range θ_S and the main lobe width $\theta_{3\,\mathrm{dB}}$

$$\Delta R = \frac{c}{2B'} = \frac{c}{2B} \cdot \frac{\theta_s}{\theta_{3\,dB}}. \tag{2}$$

The linear relationship between the resulting beat frequency and the target distance remains fundamentally preserved. Accordingly, the distance R to the target is given by [6], [7]

$$R = \frac{c}{2B} \cdot (f_{beat} \cdot t_{mod}). \tag{3}$$

B. Tradeoff Between Angular and Target Resolution

From the preceding discussion, it becomes evident that optimizing the target resolution requires a wide frequency range, which in turn demands a broader antenna main lobe width. In contrast, the precise angle determination necessitates a narrowly focused beam resulting in low-target resolution. These opposing requirements give rise to a fundamental conflict when combining FMCW radar with frequency-steered antenna scanning techniques. Rearranging (2) yields an uncertainty relation that describes the product of the target and angular resolutions

$$\Delta R \cdot \theta_{3\,\mathrm{dB}} = \frac{c}{2B} \cdot \theta_S. \tag{4}$$

This relationship clearly demonstrates that improving one parameter necessarily degrades the other. Thus, for a given

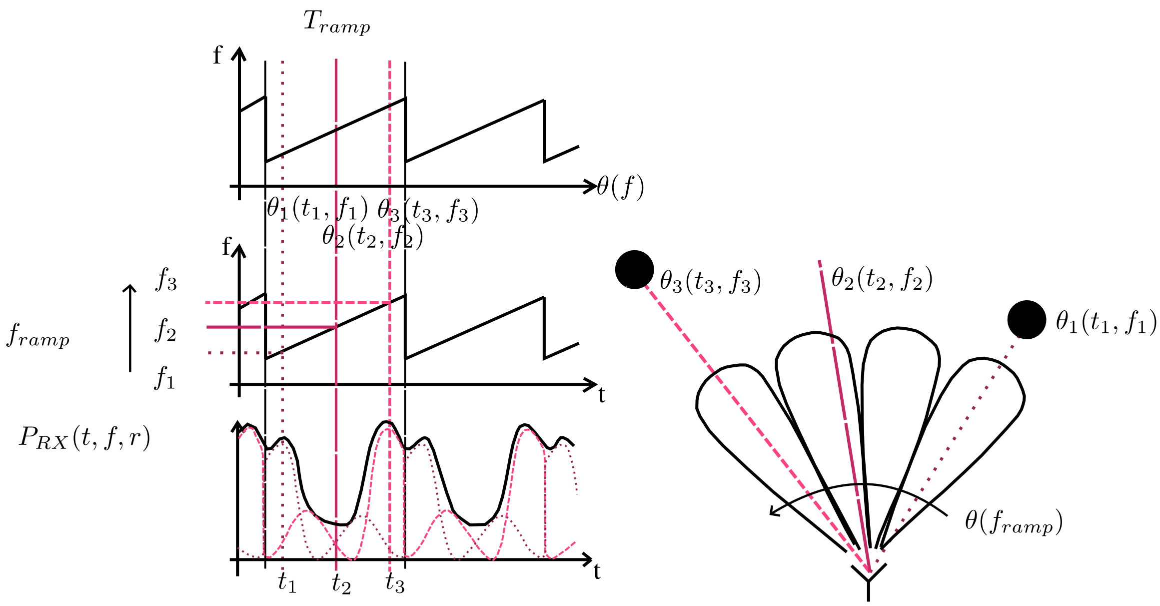

Fig. 1. Illustration of an FMCW radar with a frequency-steered antenna.

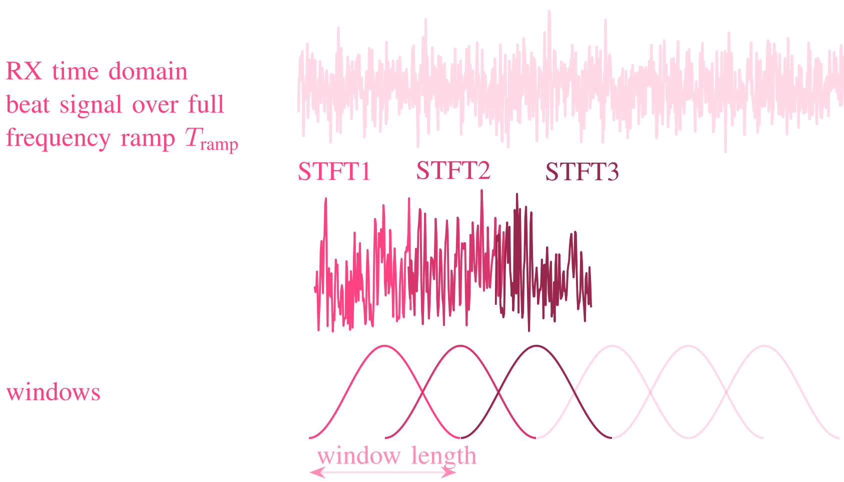

Fig. 2. Signal processing using STFT analysis.

theoretical limit on target resolution, the corresponding limit on angular resolution can be determined. This close interdependence imposes specific requirements on the system architecture, which must facilitate an optimal compromise between target and angular resolution. In particular, the choice of antenna technology plays a central role in achieving the desired performance. The parameters of the LWA will also influence the subsequent signal processing [8], [9].

III. Signal Processing

For signal evaluation, the received signal is continuously analyzed using a short-time Fourier transform (STFT), which enables the examination of the frequency domain in time-limited segments (see Fig. 2). The constrained illumination of the target during the beam squint only allows the effective bandwidth B' to deliver the range information. Hence, for a given HPBW of the main lobe, B' is well defined by the squint relation angle over frequency span, allowing to calculate the target range by an STFT analyzing this effective bandwidth. In addition, the squinting beam defines the time span a target is illuminated, which puts constraints on the frequency resolution of the STFT in terms of its length. This bandwidth is required to calculate the radial distance covered by a target in each ramp segment during scanning. As shown in Fig. 2, the time-domain signal is sequentially divided into STFT windows, discretizing the angles according to the window length, corresponding to the number of windows needed for the entire frequency ramp. Each window thus enables the separation of targets in the range domain and provides more precise distance measurements. During azimuth scanning with a frequency ramp of the transmitted signal, the HPBW determines the duration of target illumination and, consequently, the angular resolution. The ultimate goal is to maximize the proportion of the available bandwidth B' that is effectively used for target illumination within the currently illuminated angle, while maintaining a narrow beam for good angular resolution. However, this is inherently in conflict with the desire to generate a total scan angle as wide as possible using the entire available bandwidth B. This tradeoff forms the basis for the following antenna requirements. The proposed STFT-based angle estimation can be interpreted as a spectral beamforming process that is closely related to classical FFT-based digital beamforming. In conventional beamforming, an FFT across spatial channels maps the spatial frequency to the cosine of the angle of arrival. In the presented concept, the FFT (or STFT) is applied to the FMCW beat signal to estimate the instantaneous frequency, which is then mapped to discrete angular sectors via the known frequency–angle characteristic of the LWA. Consequently, the angle estimation is performed through a deterministic lookup rather than spatial phase differences, while relying on the same underlying spectral estimation principles. From a system perspective, this implies that the angular resolution and robustness of the proposed approach are governed by the same fundamental factors as in classical beamforming. Multiple targets are resolved based on their separability in the spectral domain, and performance degrades with decreasing SNR, strong multipath components, or closely spaced targets with differing radar cross sections. These effects do not arise from the antenna concept itself but from the spectral estimation process and the radar signal model, and are therefore comparable to those observed in FFT-based digital beamforming systems.

IV. Antenna Requirements

LWAs are particularly well-suited for angle-dependent frequency scanning, and their performance improves significantly with increasing operational bandwidth. As indicated by (4), systems aiming to exploit beam squinting must prioritize large bandwidths to ensure sufficient angular resolution. Since such bandwidths are typically only achievable at higher frequencies, the 60-GHz ISM band presents itself as an ideal choice. For this reason, the antenna is designed to operate around 61 GHz, where commercial radar chipsets with high bandwidth are readily available. Specifically, the Infineon BGT60TR13 radar chipset, featuring one transmit and three receive channels in an L-shaped configuration, provides a usable bandwidth of 5.5 GHz, which aligns well with the antenna's requirements and supports reliable angle estimation across the desired frequency range. In addition to bandwidth and angular resolution requirements, a sufficient antenna gain is required to ensure reliable target detection in short-range radar scenarios. Based on a radar link budget analysis for human target detection at distances up to 5.5 m in the 60-GHz band, a minimum transmit antenna gain of at least 8 dBi is specified. This ensures an adequate signal-to-noise ratio for robust detection performance while maintaining a compact antenna geometry. For this reason, we have designed two antennas: one primarily targeting high-range resolution in [10], and the one presented in this work, optimized for enhanced angular resolution. Additional important design criteria include a compact form factor with an antenna length below 10 cm, cost efficiency, and a flexible configuration that allows the antenna to be adapted to different application scenarios. To avoid high losses, a waveguide-based implementation is pursued instead of a planar printed circuit board design, as this design offers low-loss values and high power transfer due to its physical properties, and it can be cost-effectively produced via 3-D printing. In addition, the antenna should be manufactured in a single piece to prevent inaccuracies during assembly that could adversely affect the high-frequency properties. Despite different optimization focuses, a minimum beam steering range of 40° remains essential for short-range sensing applications.

A. Slotted Radiators LWAs

A slotted radiator is essentially a waveguide in which multiple slots are introduced in its wall to deliberately radiate electromagnetic energy. The arrangement of multiple slots results in an array antenna, referred to as a slotted waveguide array antenna (SWAA) [11], [12].

The performance of this antenna is based not only on the self-admittance of the individual slots but also on the mutual admittances between adjacent slots. Therefore, the active admittance for each slot is defined as follows:

$$Y_{a,n} = Y_{nn} + Y_{b,n} \tag{5}$$

where Y_{nn} represents the self-admittance of the nth slot and $Y_{b,n}$ is the sum of the couplings (mutual admittances) to all other slots. The geometric spacing d between the slots plays a crucial role in the radiation behavior. For a given guided wavelength λ_g inside the waveguide and for fixed geometrical distances d between the slots, the effective electrical length between the slots relates to the phase propagation constant β. This leads to a sweep of the phases at the radiating slots along the waveguide. Therefore, two general configurations can be distinguished concerning the radiation characteristics of the slotted array.

1) *Standing-Wave Fed Array ($d = \lambda_g/2$):* At this spacing, the wall currents of adjacent slots flow in exactly opposite directions. To avoid mutual cancellation of the fields, the slots are alternately placed on opposite sides of the centerline of the waveguide wall, resulting in an additional phase shift of 180°. Consequently, all slots radiate in phase, and the main beam of the antenna points perpendicularly (broadside) to the plane of the slots. This is the common and intended operation for many arrays and only holds true for narrowband operation, i.e., a slight variation of λ_g within the used bandwidth.

2) *Traveling-Wave Fed Array ($d \neq \lambda_g/2$):* Here, the slightly different slot spacing d leads to a phase difference between the slots. The resulting phase difference is frequency-dependent, as the propagation constant (phase constant) β of the waveguide mode varies according to

$$\beta = \frac{2\pi}{\lambda_g} = \sqrt{\left(2\pi f\sqrt{\mu_0\epsilon_0}\right)^2 - \left(\frac{\pi}{a}\right)^2} \tag{6}$$

based on [13], where λ_g is the guided wavelength inside the waveguide, f is the operating frequency, μ_0 and ϵ_0 are the permeability and permittivity of free space, and a represents the waveguide width. For a periodic array, the condition for constructive radiation of the mth Floquet harmonic is given by

$$kd\cos\phi - \beta d = 2\pi m \tag{7}$$

where $k = 2\pi/\lambda$ is the free-space wavenumber, d is the slot spacing, β is the waveguide phase constant, ϕ is the radiation

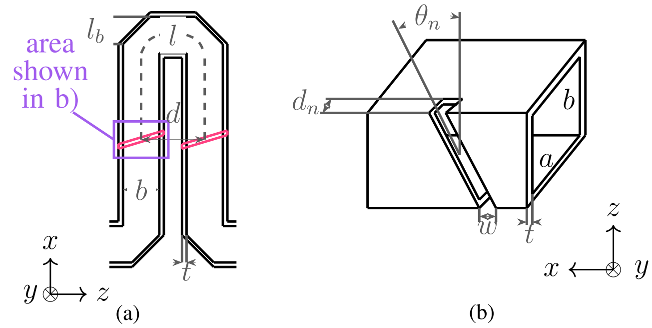

Fig. 3. Overview of (a) relevant geometric dimensions of the waveguide in the serpentine design and (b) corresponding slots.

angle, and m is an integer representing the Floquet space harmonic. Solving for the radiation angle ϕ yields

$$\phi = \arccos\left(\frac{\beta}{k} + \frac{2\pi m}{kd}\right) = \arccos\left(\frac{\beta}{k} + m\frac{\lambda}{d}\right). \tag{8}$$

In practice, for LWAs, the -1 Floquet harmonic ($m = -1$) is typically chosen, since it represents the radiating spatial harmonic. Substituting $m = -1$ into (8) gives

$$\phi = \arccos\left(\frac{\beta}{k} - \frac{\lambda}{d}\right). \tag{9}$$

Furthermore, if the slots are alternately displaced on opposite sides of the waveguide centerline to maintain in-phase radiation, the effective electrical period doubles to $2d$, leading to the final design formula

$$\phi = \arccos\left(\frac{\beta}{k} - \frac{\lambda}{2d}\right) \tag{10}$$

used by [13].

V. Design of the Serpentine Antenna

According to (10), the radiation angle of a traveling-wave-fed array antenna is determined by the ratio β/k. With an element spacing of $d = 2.38$ mm, this results in a radiation angle of $\theta_0 = 111.1°$ at 58 GHz and $\theta_0 = 102.4°$ at 63.5 GHz, yielding a frequency-dependent beam squint of only 8.7°. To extend the usable angular range and enhance angular resolution, a *serpentine design* is employed, in which the signal path is intentionally lengthened by a meandering line geometry. Fig. 3 shows the unit cell of the serpentine structure. The elongated distance $l > d$ between adjacent radiating elements increases the sensitivity of the phase constant β to frequency variations, enabling a significantly greater beam steering range within the operating band. The main beam angle θ_0 of a serpentine-structured slot-waveguide array antenna (SWGAA) is given according to [13] by

$$\theta_0 = \arccos\left(\frac{\beta l - 2\pi\left(m + \frac{1}{2}\right)}{kd}\right) \tag{11}$$

where l denotes the physical path length between two radiating elements. The design objective is to select l such that the beam angle, starting from $\theta_0 \approx 85°$, shifts further away from broadside toward 0° as frequency increases [13], [15].

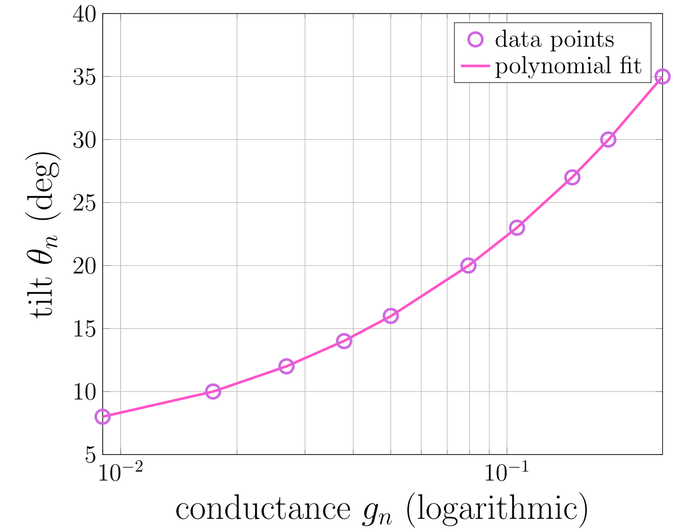

Fig. 4. Simulation results and polynomial fits for $\theta_n(g_n)$. Tilt angle versus conductance.

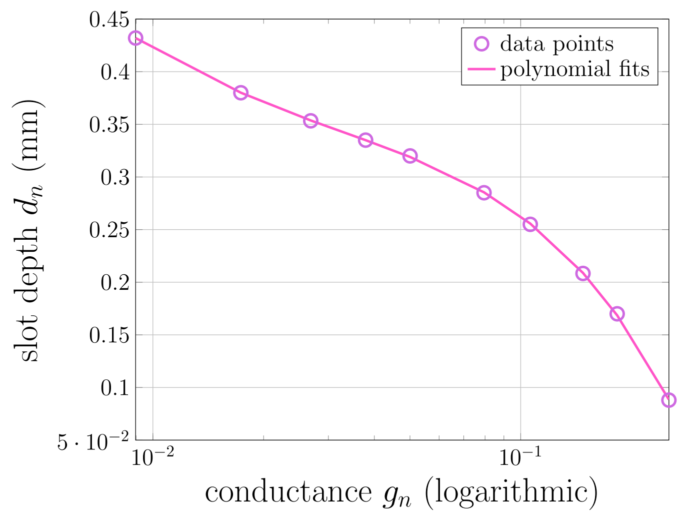

Fig. 5. Simulation results and polynomial fits for $d_n(g_n)$. Slot depth versus conductance.

Following [15], the interelement spacing must satisfy the grating-lobe condition for $f_{\max} = 63.5$ GHz to:

$$d < \frac{\lambda_0}{2} \quad \Rightarrow \quad d < 2.36\,\text{mm}. \tag{12}$$

The distance d is composed of the waveguide width b, two wall thicknesses t, and an air gap. To ensure the antenna can be physically fabricated, the air gap plus two wall thicknesses must be at least 0.5 mm. Thus, the practical slot spacing becomes

$$d = b + 0.5\,\text{mm} = 2.38\,\text{mm} \tag{13}$$

which, according to full-wave simulations, does not result in significant grating lobes. For $m = 1$, $d = 2.38$ mm, and a beam angle of $\theta_0 = 86°$ at $f = 58$ GHz, (11) yields

$$l = 10.9\,\text{mm} \tag{14}$$

which results in a beam angle of $\theta_0 = 53.8°$ at $f = 63.5$ GHz. This corresponds to a beam scanning range of 32.2°, which can be extended to ±36.2° by employing symmetric feeding (for details see Section V-B). The radiated power of each slot is controlled via its tilt angle θ_n and slot depth d_n, which define the excitation coefficients a_n. To achieve a sidelobe suppression of 20 dB, the coefficients for $N = 16$ radiating elements are derived using a Dolph–Chebyshev amplitude distribution. The choice of both the number of radiating elements and the applied amplitude taper represents a fundamental design tradeoff in frequency-scanned LWAs. Increasing the number of slots generally results in a narrower main beam and improved angular selectivity, but simultaneously increases the overall antenna length, fabrication complexity, and sensitivity to manufacturing tolerances. Conversely, a reduced number of elements improves compactness and robustness, but leads to elevated sidelobe levels and reduced directivity. Based on these considerations, the number of elements was set to $N = 16$ as a compromise among angular resolution, sidelobe suppression, and practical realizability. Parametric simulations indicate that configurations with fewer than 16 elements exhibit significantly increased sidelobe levels over the operational frequency band, while larger arrays provide only marginal improvements in main-beam characteristics at the cost of increased sensitivity to fabrication-induced deviations and accumulated phase errors. In particular, small variations in slot depth or tilt angle increasingly affect the radiation pattern for larger values of N, resulting in pronounced sidelobe degradation and beam distortion. The Dolph–Chebyshev amplitude taper was selected due to its well-defined optimality: for a prescribed maximum sidelobe level, it yields the narrowest possible main beam. This property is especially beneficial in frequency-steered antennas, where stable sidelobe behavior over a wide frequency range is critical. Alternative tapers, such as uniform or Taylor distributions, were evaluated in simulation but were found to either provide insufficient sidelobe suppression across the scan range or require a larger number of elements to achieve comparable performance. Consequently, the Dolph–Chebyshev taper offers a favorable balance among sidelobe control, scan linearity, and robustness against fabrication tolerances. The normalized array factor is given by

$$(\mathrm{AF})_{2M} = \sum_{n=1}^{M} a_n \cos\left[(2n-1)\,\tfrac{\psi}{2}\right], \quad \psi = kd\cos\phi - \beta l. \tag{15}$$

The corresponding conductance values are calculated as follows:

$$g_n = \frac{a_n^2}{\sum_{i=1}^{N} a_i^2}. \tag{16}$$

For each g_n, the corresponding values of $\theta_n(g_n)$ and $d_n(g_n)$ are obtained through full-wave simulations in CST Microwave Studio (see Figs. 4 and 5). These results are approximated by fourth-order polynomial fits

$$\begin{aligned}\theta_n(g_n) = {} & 0.020\,(\log g_n)^4 + 0.479\,(\log g_n)^3 + 5.353\,(\log g_n)^2 \\ & + 28.877\log g_n + 65.765 \end{aligned} \tag{17}$$

$$\begin{aligned}d_n(g_n) = {} & -0.003\,(\log g_n)^4 - 0.047\,(\log g_n)^3 - 0.302\,(\log g_n)^2 \\ & - 0.877\log g_n - 0.660. \end{aligned} \tag{18}$$

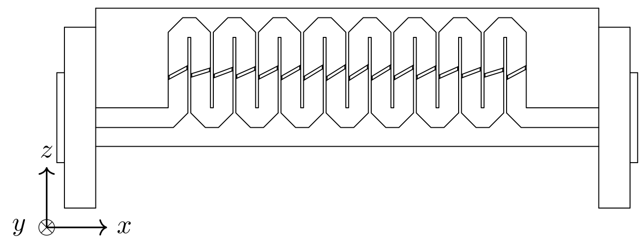

Fig. 6. Sketch of the LWA with serpentine design and a total size of 4.48 cm between the waveguide flanges.

TABLE I
OVERVIEW OF THE SLOT PARAMETERS

Slot n	Excitation coefficient a_n	Conductance g_n	Tilt angle θ_n (deg)	Slot depth d_n (mm)
1	0.866	0.069	18.731	0.296
2	0.504	0.023	11.332	0.361
3	0.621	0.035	13.656	0.338
4	0.733	0.049	15.947	0.319
5	0.832	0.064	18.017	0.302
6	0.913	0.077	19.710	0.287
7	0.970	0.087	20.907	0.276
8	1.000	0.092	21.526	0.270
9	1.000	0.092	21.526	0.270
10	0.970	0.087	20.907	0.276
11	0.913	0.077	19.710	0.287
12	0.832	0.064	18.017	0.302
13	0.733	0.049	15.947	0.319
14	0.621	0.035	13.656	0.338
15	0.504	0.023	11.332	0.361
16	0.866	0.069	18.731	0.296

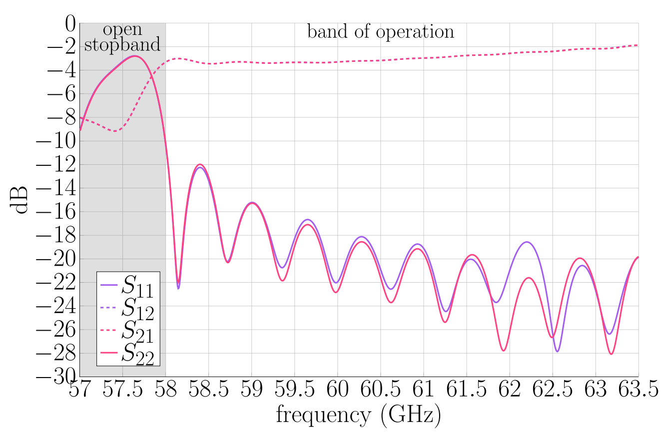

Fig. 7. S-parameters of the initial simulation model (see Table I).

The slot width is determined following [11] as:

$$w = \frac{1}{16} \cdot \frac{a}{0.9} = 0.261\ \mathrm{mm}. \tag{19}$$

The computed values for a_n, g_n, θ_n, and d_n are summarized in Table I. A sketch of the designed LWA is shown in Fig. 6.

A. Simulation of the LWA

Using these parameters, the 3-D model was created in CST Microwave Studio. The simulation shown in Fig. 7 exhibits an efficiency between −5.2 and −3.1 dB, mainly due

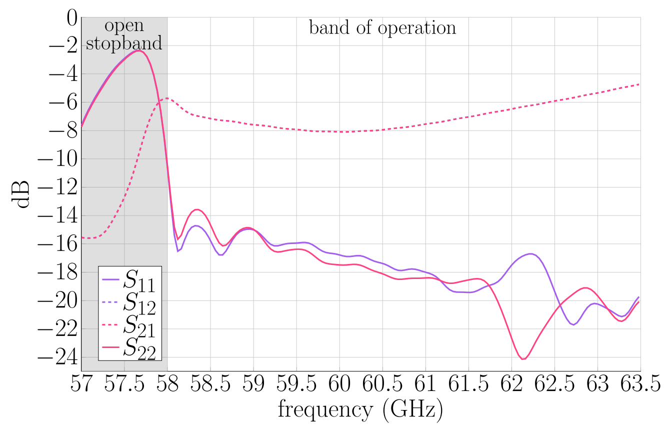

Fig. 8. S-parameters of the adjusted simulation model (see Table II).

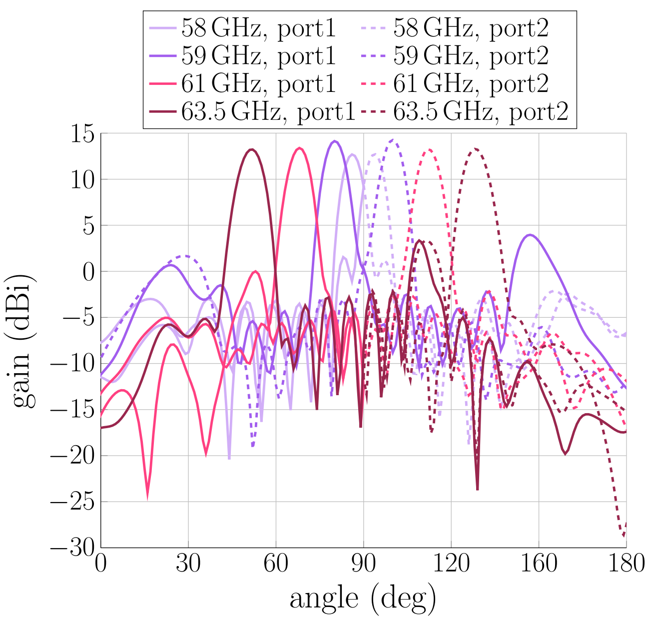

Fig. 9. Far-field simulation of the antenna at both ports in the frequency range of 58–63.5 GHz.

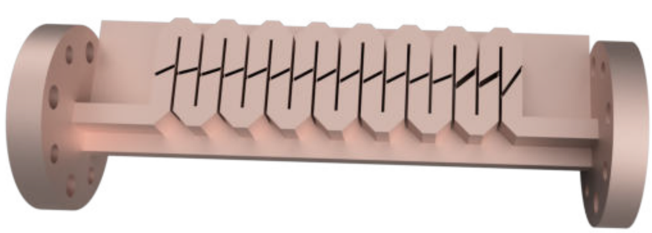

Fig. 10. CAD model of the modified antenna structure with intentionally introduced geometric asymmetry to reduce the OSB effect.

to a high transmission with $S_{21} \approx -3$ dB. To improve the radiated power, all tilt angles were scaled by a factor of 1.5 ($\theta_{n,adj} = 1.5\theta_n$), and the corresponding new slot depths $d_{n,adj}$ were calculated using the polynomial fit

$$d_n(\theta_n) = 1.5 \times 10^{-6}\theta_n^4 - 0.0001508\theta_n^3 + 0.0051532\theta_n^2 - 0.0819125\theta_n + 0.8250823. \quad (20)$$

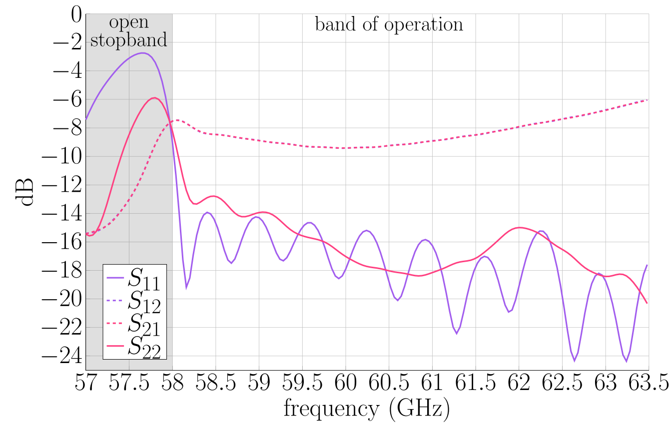

Fig. 11. Simulated scattering parameters of the modified antenna model, as shown in Fig. 10.

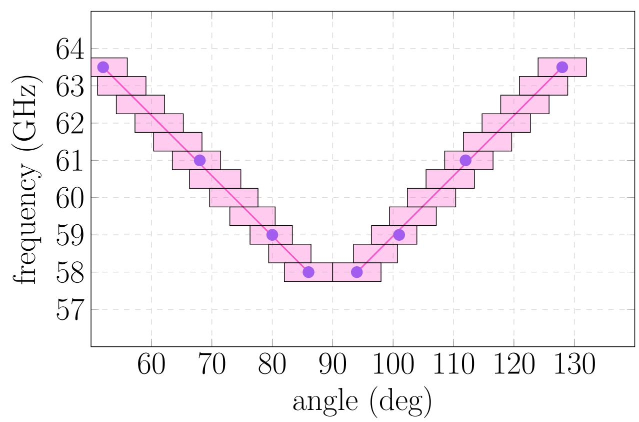

Fig. 12. Simulated frequency–angle relationship of the serpentine LWA, illustrating the linear beam squint and the angular coverage of both ports across the operational frequency band.

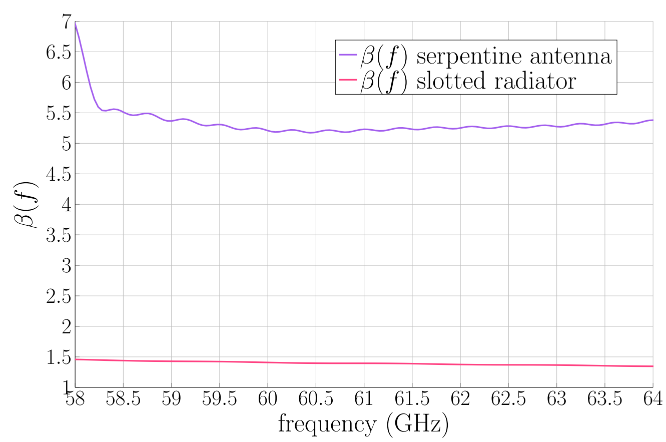

Fig. 13. Comparison of the dispersion curve $\beta(f)$ between a conventional slotted radiator and the serpentine LWA.

The slot width was increased to $w_{adj} = 0.34$ mm to compensate for manufacturing tolerances. The adjusted slot parameters are summarized in Table II. After the adjustment, S_{21} decreases to approximately −6.5 dB, while S_{11} remains below −15 dB in the frequency range from approximately 58 to 63.5 GHz, which corresponds to the relevant operating band of the proposed radar system (see Fig. 8). Outside this band, a pronounced degradation of the impedance matching can be

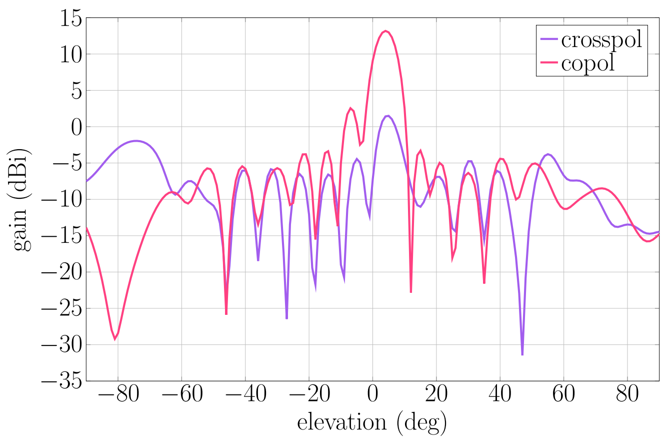

Fig. 14. Simulated co- and cross-polarized radiation characteristics of the proposed LWA in the main beam direction.

observed. In particular, between 57 and 58 GHz, S_{11} locally increases to values of up to about −2 dB. This behavior is associated with the so-called open-stopband (OSB), which occurs in periodic LWAs in the vicinity of the broadside condition. In this frequency region, the effective power transfer along the structure is disturbed, which primarily manifests itself as a deterioration of the impedance matching. Since this effect occurs outside the intended operating band, it does not adversely affect the overall system performance. The efficiency improves to values between −2.4 and −0.87 dB, while the beam steering remains at approximately 34° per port. By exciting the antenna from both ports, the beam scans across the broadside region in opposite directions, resulting in a total angular coverage of about 76° (see Figs. 8 and 9). This total coverage is determined by the extreme beam directions of both excitations and is slightly larger than twice the single-port scanning range, as the beams overlap around broadside within their half-power beamwidth rather than exactly at their maxima. Each port operates over a frequency range of approximately 5.5 GHz, corresponding to an average scanning sensitivity of about 7°/GHz. By exciting the antenna from both ports, the full angular coverage of 76° can be achieved while using only the 5.5-GHz bandwidth per port. Beyond the scattering parameters, a local degradation of the realized gain is observed in the broadside region around $\theta \approx 90°$. This behavior is characteristic of periodic LWAs and is commonly referred to as the OSB phenomenon. It occurs when the phase constant of the guided mode approaches $\beta \approx 0$, where the forward and backward spatial harmonics couple and the radiated power is partially redistributed instead of being efficiently radiated. In the present antenna, this manifests itself as a localized reduction in radiation efficiency and realized gain within a narrow frequency interval around the broadside condition. Outside this region, the antenna exhibits stable radiation characteristics with a nearly constant realized gain. In periodic LWAs, the OSB is commonly mitigated by introducing intentional asymmetries in the unit cell, for example, by using staggered slots, unequal perturbations, or different radiating element geometries. Such measures disturb the symmetry of the periodic structure and prevent the formation of a standing-wave condition near $\beta \approx 0$. In the present work, however, a left–right symmetric antenna geometry was intentionally maintained. This symmetry is essential for the dual-port excitation concept employed in the proposed radar system, where the antenna is fed alternately from both ends in order to cover the full-angular scanning range. Introducing structural asymmetries in the unit cell would shift the dispersion characteristics of the structure and could lead to different radiation behaviors depending on the excitation port, thereby degrading the symmetry of the beam scanning and potentially affecting both the achievable squint and the linearity of the frequency–angle relationship. Nevertheless, several design aspects already contribute to a partial reduction of the OSB effect. In particular, the traveling-wave radiation along the slot array, the finite length of the antenna, and the applied amplitude tapering reduce the strength of the standing-wave interaction that typically amplifies the OSB in ideal infinite periodic structures. As a result, the OSB does not lead to a complete radiation suppression in the present design but only to a moderate reduction of the realized gain in the broadside region. To further illustrate this design tradeoff, an additional comparison model is shown in Fig. 10. In this modified antenna, the slot geometry on one side of the structure was intentionally altered by increasing the slot width and rotation angle in order to disturb the symmetry and reduce the OSB. The corresponding scattering parameters of this modified structure are depicted in Fig. 11. It can be observed that the S-parameters become clearly asymmetric due to the introduced geometric perturbation. At the same time, the OSB effect is noticeably reduced. In particular, the reflection coefficient at the second port improves significantly, with the maximum of S_{22} decreasing from approximately −2 dB in the symmetric design to about −6 dB in the modified structure. This indicates a substantial mitigation of the OSB effect. However, the introduced asymmetry also leads to unequal scattering parameters at the two ports, which implies different antenna behavior depending on the excitation side. As a consequence, the radiation characteristics become dependent on the excitation port, which contradicts the fundamental design requirement of symmetric dual-port operation. For this reason, such asymmetric OSB mitigation techniques were not adopted in the final antenna design. In the intended radar setup, the receiving antenna is realized as a horn antenna, which inherently provides its maximum gain in the forward direction and exhibits a gradual gain reduction toward the edges of its radiation pattern. As a result, the influence of the reduced transmit gain of the LWA in the vicinity of broadside is partially reduced in the overall system response. Consequently, an explicit suppression of the OSB was not required for the targeted application. The resulting antenna configuration provides a sufficiently uniform angular sensitivity over the scanning range, which is beneficial from a radar system perspective, as it limits strong variations in received signal levels across different look angles. The linearity simulation (see Fig. 12) illustrates the dependence of the radiation angle on frequency for both ports of the LWA. The results exhibit an almost perfectly linear dispersion, with frequencies from 58 to 63.5 GHz following the expected squint behavior. The width of the pink boxes represents the antenna's HBPW, providing

TABLE II
OVERVIEW OF THE ADJUSTED SLOT PARAMETERS

Slot n	Adjusted tilt angle $\theta_{n,adj}$ (deg)	Adjusted slot depth $d_{n,adj}$ (mm)
1	28.097	0.195
2	16.998	0.308
3	20.484	0.281
4	23.921	0.248
5	27.026	0.210
6	29.566	0.173
7	31.361	0.145
8	32.289	0.130
9	32.289	0.130
10	31.361	0.145
11	29.566	0.173
12	27.026	0.210
13	23.921	0.248
14	20.484	0.281
15	16.998	0.308
16	28.097	0.195

a visual indication of beam spread. These simulation results confirm that the phase and amplitude distributions along the antenna are designed to produce a linear angle–frequency relationship, which is essential for its intended operation as an single input single output (SISO) radar. It is evident that each port independently covers distinct angular regions and that the dispersion remains nearly uniform across the examined frequency range. Fig. 13 shows the dispersion characteristic $\beta(f)$ as a function of frequency for the conventional slotted radiator and the serpentine LWA. While the conventional slotted radiator exhibits a relatively flat and low phase constant, the serpentine structure shows a stronger frequency-dependent dispersion. Due to the longer signal path between the radiating elements, the phase constant β becomes more sensitive to frequency variations, enabling a larger beam scan within the operating band. At the same time, the dispersion of the serpentine antenna remains nearly linear, so the desired beam direction per port stays consistent and the angular resolution is not degraded. This property allows a controlled extension of the usable beam angle, which is essential for implementing the overall concept. In addition to the dispersion behavior, the polarization properties of the antenna are discussed. This design approach inevitably introduces a certain level of cross-polarized radiation (see Fig. 14). However, cross-polarization was not a primary optimization target in the present design, as it is not critical for the intended radar application. The cross-polarization level is evaluated based on the standard co- and cross-polarization definition in the far field by decomposing the radiated electric field into orthogonal polarization components with respect to the main polarization direction of the antenna. The cross-polarization discrimination (XPD) is defined as follows:

$$\mathrm{XPD} = 10\log_{10}\left(\frac{|E_{\mathrm{co}}|^2}{|E_{\mathrm{cross}}|^2}\right). \tag{21}$$

Full-wave simulations show a co-polarized gain of approximately 12.5 dBi and a cross-polarized gain of about 2.5 dBi in the main beam direction, corresponding to an XPD of roughly 10 dB. This behavior is consistent over the relevant frequency range and confirms that the cross-polarized field component remains clearly suppressed with respect to the desired polarization. For the radar-focused application addressed in this work, the achieved cross-polarization level is sufficient and does not impose a limitation on system performance. To complement the previously introduced conceptual schematics in Fig. 1, Fig. 15 provides a frequency- and angle-resolved illustration of the proposed FMCW radar concept using the simulated characteristics of the presented antenna. While the general operating principle is independent of the absolute frequency range and beam angles, this figure explicitly maps the frequency sweep to the corresponding radiation angles obtained for the designed serpentine LWA. The annotated frequencies and angles illustrate how individual frequency points within the FMCW ramp correspond to distinct spatial directions, thereby linking the abstract beam-squinting concept to the actual operating band of 58–63.5 GHz. This representation clarifies the relationship among frequency, beam direction, and angular coverage for both antenna ports and directly reflects the simulated dispersion and radiation characteristics discussed in Section IV.

B. Principle With Switch

To increase the effective bandwidth, the antenna is designed to utilize both available ports. By employing a waveguide switch (see Fig. 16), the feed points are alternately activated within a defined time interval. The switching inverts the propagation direction of the feeding wave and thus the phases at the radiating slots. Since the antenna geometry is strictly symmetric, the beam tilts in the opposite direction if the switch feeds the other port. In this way, the physically available bandwidth of 5.5 GHz is transformed into a virtual sweep bandwidth of 11 GHz for the effective range of squinting by sequentially using two distinct frequency ranges for target sampling. This doubling of the virtual bandwidth improves the range resolution, as more bandwidth per target is available during scanning. With a bandwidth step size of, for example, $B' = 500$ MHz, this setup enables a range resolution of $\Delta R = 30$ cm according to (1). To ensure an even utilization of both ports, the antenna is designed symmetrically and equipped with flanges at both ends. In addition, the waveguide elbows have been integrated to facilitate the precise mounting of the switch between the antenna flanges (see Fig. 16). Alternatively, a radar chipset with two TX channels can be used to reduce the overall size and weight of the system while maintaining its core functionality.

C. Fabrication and Metallization of the Antenna

The antennas are fabricated using a *Form 3+* SLA 3-D printer (*FormLabs*), where liquid resin is selectively cured layer by layer with a laser to produce fine and smooth surface structures [16]. Clear resin with a layer thickness of 25 μm is used for printing. The print quality is strongly influenced by the orientation of the antenna during the additive manufacturing process. The most favorable results in terms of layer adhesion and minimization of support structures were achieved when the antenna was tilted by approximately 5° relative to the

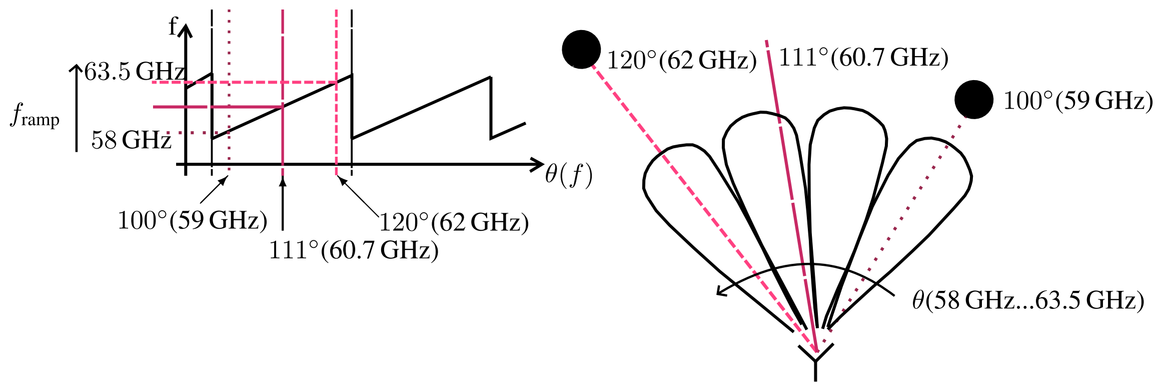

Fig. 15. Frequency- and angle-resolved illustration of the FMCW radar principle using the simulated beam steering characteristics of the proposed serpentine LWA.

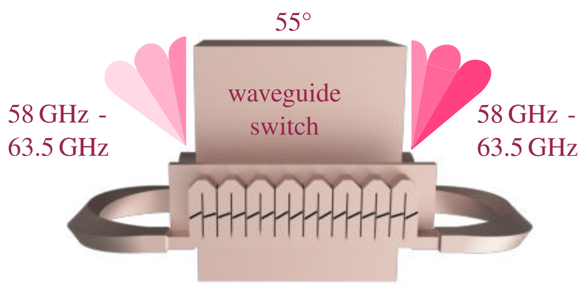

Fig. 16. Overview of the complete concept with a waveguide switch.

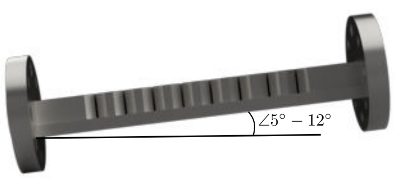

Fig. 17. Tilt angle of the antenna base plate relative to the build platform (side view).

build platform (confer Fig. 17). To further optimize the print quality, various tilt angles of the antenna with respect to the build platform were investigated. In SLA printing, the inclination angle has a significant impact on dimensional accuracy, surface quality, and mechanical stability. If the part is printed nearly horizontally, the so-called *suction cup effect* can occur, a strong vacuum between the part and the FEP film, which can lead to vibrations, layer shifts, and microcracks during the peeling of each layer. In addition, a flatter orientation increases the simultaneously exposed area, potentially causing uneven curing and higher mechanical stress during the detachment process. Conversely, at steep angles (greater than 20 °), the edge quality deteriorates due to pronounced staircase effects. Within a range of 5 °–12 ° (confer Fig. 17), the best print quality was observed in terms of geometric fidelity and process stability.

Despite the fine resolution, residual resin remains inside the narrow slots after standard cleaning in the *Form Wash* system due to capillary forces. An additional cleaning step with isopropanol and compressed air is necessary to fully expose the structures. Subsequently, final curing is performed in a UV-light station (*Form Cure*). To enable the antenna to radiate, metallization is carried out using the Tollens' reaction, which, unlike electroplating, does not require initial electrical conductivity. After precleaning with demineralized water, the antennas are immersed in an activation solution consisting of stannous chloride, hydrochloric acid, and water. This treatment forms active nucleation sites on the surface, facilitating subsequent silver deposition. After thorough rinsing, the silver coating is performed. To metallize the antenna surface, a chemical silver deposition process based on Tollens' reaction was employed. All steps were conducted under a fume hood to ensure safe handling of the reagents. The process consisted of the following stages.

First, the reducing agent solution was prepared by dissolving 1.5 g of dextrose ($C_6H_{12}O_6$) in 30 mL of deionized water. Subsequently, Tollens' reagent was prepared by dissolving 1.5 g of silver nitrate ($AgNO_3$) in 75 mL of deionized water. To this solution, 0.3 g of sodium hydroxide ($NaOH$), previously dissolved in 75 mL of water, was added. Ammonium hydroxide (30 % NH_4OH) was then incrementally introduced until the solution turned transparent, indicating the formation of the diamminesilver(I) complex. The printed antennas were fully immersed in the prepared Tollens' reagent, and any air bubbles trapped in narrow geometries were removed by magnetic stirring. While maintaining agitation, the dextrose solution was slowly added to the reaction bath, initiating the reduction of silver ions and the formation of a conformal metallic silver layer on the antenna surface. The deposition process typically lasted between 1 and 5 min, depending on the geometric complexity and slot dimensions. To enhance the surface conductivity and reduce ohmic losses, the silver deposition cycle was repeated three times. After each metallization step, the antennas were thoroughly rinsed with deionized water to remove any residual reagents.

D. Improvement by Pump-Assisted Metallization

To optimize the metallization of the serpentine antenna, two approaches were compared. In the first method, the antenna was immersed in Tollens' reagent under magnetic stirring. In the second approach, the reagent was actively pumped through the hollow waveguide using a peristaltic pump, creating a

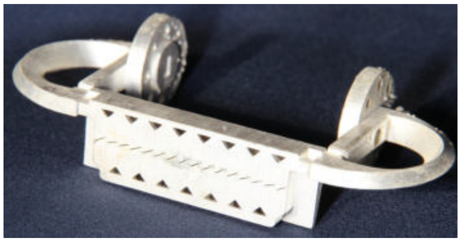

Fig. 18. 3-D-printed serpentine antenna after silver coating.

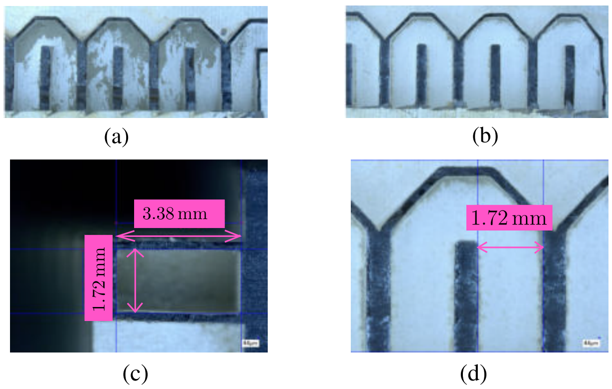

Fig. 19. Microscopic images of the LWA. (a) Without a peristaltic pump. (b) With a peristaltic pump. (c) Measured waveguide width. (d) Measured waveguide height.

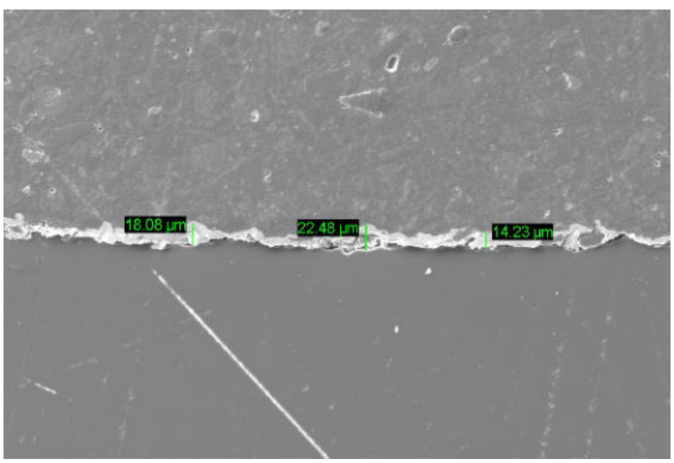

Fig. 20. SEM cross-section image of the metallized structure showing a continuous silver layer with a thickness varying between approximately 14 and 22 μm.

closed-loop system: the reagent was circulated through the slots and returned along the opposite side of the antenna. The fully metallized LWA is shown in Fig. 18.

A comparison of Fig. 19(a) and(b) showing a serpentine section cut open demonstrates that the use of a peristaltic pump significantly reduces contamination within the serpentine structure. Without active circulation, deposits tend to accumulate in the bends, effectively shortening the total serpentine length l.

The microscopic images in Fig. 19(c) and (d) further illustrate the print quality. No air gaps between adjacent serpentine loops are visible. The measured waveguide dimensions a = 3.38 mm and b = 1.72 mm are slightly smaller than the nominal WR15 waveguide dimensions designed in the 3-D model (a = 3.76 mm and b = 1.88 mm). To compensate for this deviation, the model was revised prior to the final print: the serpentine length was increased by 200 μm per half loop, and the width of the waveguide opening was enlarged by 100 μm. As a result, the printed structure eventually matched the intended dimensions. While the visual and dimensional quality improvements are evident, it is worth noting that even small deviations in geometry or surface characteristics due to the manufacturing process can lead to significant variations in antenna performance. This sensitivity necessitates a detailed process understanding and iterative refinement of both design and fabrication steps. The process presented in this work reflects such an optimization, offering a reproducible method with reduced variability and improved overall antenna performance across multiple prototypes. To further assess the quality of the metallization process, scanning electron microscope (SEM) cross-sectional images were taken, as shown in Fig. 20. The images confirm a continuous and closed metallization layer with a locally varying thickness between approximately 14 and 22 μm. The observed thickness variations are mainly attributed to the coating process and the surface topography of the additively manufactured substrate. At 60 GHz, the skin depth in silver is approximately $\delta \approx$ 0.25 μm, such that even the minimum measured thickness corresponds to more than 50 skin depths. Consequently, the RF current is fully confined within the metallization layer, and conductor losses are not limited by the metallization thickness. While surface roughness can influence conductor losses at millimeter-wave frequencies, the roughness visible in the SEM images is predominantly located at the metallization–substrate interface and is therefore separated from the current-carrying region by several tens of skin depths. The electromagnetic behavior is thus governed by the outer surface of the metallization layer. For the applied silver coating, the effective surface roughness is small compared to the skin depth and is not expected to introduce significant additional losses. As a result, neither the observed thickness variations nor the surface morphology of the metallization represents a limiting factor for the antenna performance.

E. Antenna Measurement

To determine the gain of the developed antenna, a measurement setup with a vector network analyzer (*PNA-X, Keysight*) was used. The PNA-X provides an output power of 0 dBm, with Port 1 connected to the antenna under test (DUT) and Port 2 connected to a V-band standard gain horn (24 dBi gain). Both antennas are positioned in an anechoic chamber at a distance of R = 1 m (see Fig. 21), with the DUT mounted on a motorized turntable. During rotation in the azimuthal range in 0.5° increments, the transmission factor S_{21} is measured over the frequency range from 58 to 63.5 GHz, while the input reflection coefficient $S_{11} \equiv b/a$ and S_{22} is simultaneously recorded. This measurement of S_{11} allows the PNA-X to function equivalently as an interferometric radar, providing the ratio between the transmitted and received signal and minimizing the impact of hardware imperfections

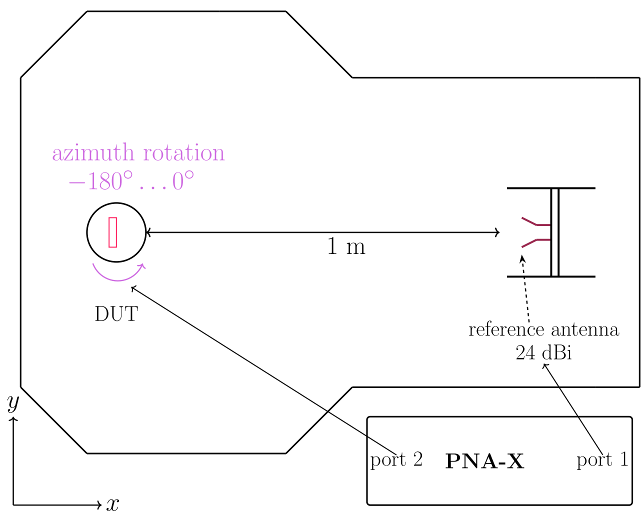

Fig. 21. Schematic of the measurement setup used for the LWA characterization.

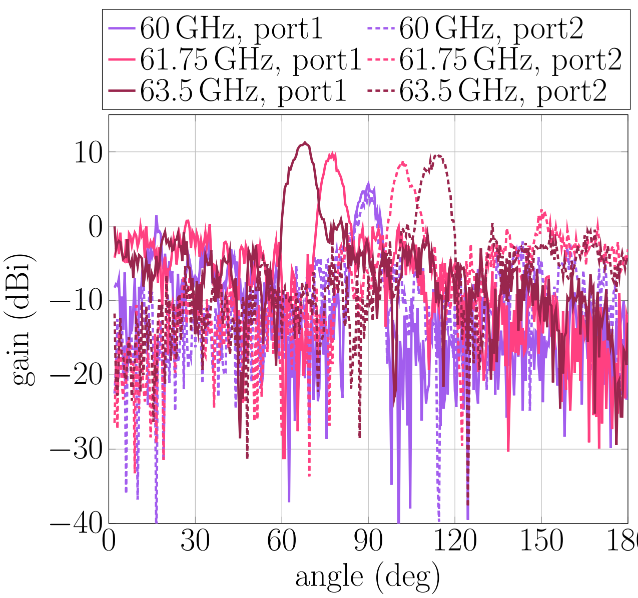

Fig. 22. Measurement results of the LWA metallized without a peristaltic pump.

by exploiting the analyzer's FMCW sweep and its internal directional coupler as an idealized radar frontend.

The receiving horn is connected to the PNA-X port via a coaxial-to-waveguide adapter, at whose coaxial reference plane a full two-port calibration using a calibration kit is performed. Pyramid-shaped absorbers are applied in the chamber to suppress spurious reflections caused by the setup.

Starting from the free-space loss at 1 m

$$D_f = 10 \log_{10} \left(\frac{5 \text{ mm}}{4\pi 1 \text{ m}} \right)^2 = -68 \text{ dB} \tag{22}$$

the gain of the DUT can be calculated using

$$G_{\text{DUT}} = P_{RX} + 44 \text{ dB}. \tag{23}$$

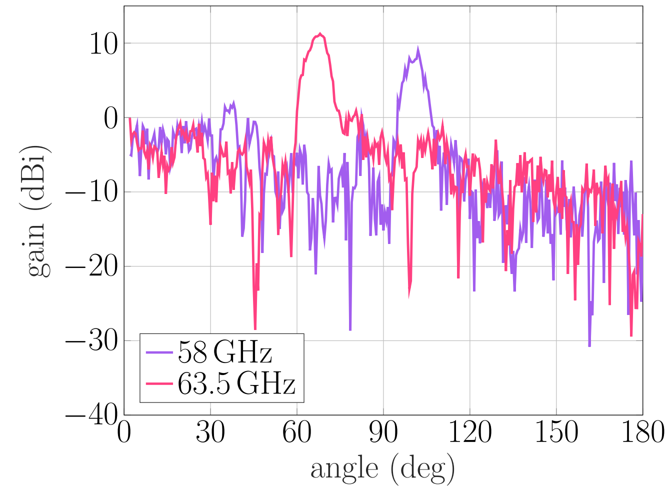

Fig. 23. Measurement results of the LWA metallized without a peristaltic pump. Main lobe beamwidth at the minimum (f = 58 GHz) and maximum (f = 63.5 GHz) frequencies.

For loss determination, a reference measurement is performed using an identical reference horn antenna instead of the DUT, yielding a maximum gain of 20.5 dBi. This results in additional measurement losses of 3.5 dB, attributed to the waveguide transitions, which are taken into account in the data analysis. The measurement results of the LWA metallized without a peristaltic pump are shown in Fig. 22. The main radiation direction at f = 58 GHz is at θ = 102° (see Fig. 23), and at f = 63.5 GHz, it is at θ = 68°, corresponding to a beam steering of 34°. The radiation direction is shifted approximately 16° to the right compared to the simulation. Overall, a beam steering of 47° is observed between θ = 68° and θ = 115°. A gain drop is observed around θ = 90°. In the measured radiation patterns, the individual frequency-dependent beams are more closely spaced in the broadside region than predicted by simulation. This leads to a reduced gain around θ = 90°, as the OSB-related gain drop occurs at a slightly shifted frequency. While simulations predict the minimum gain at approximately 57.5 GHz, the corresponding gain reduction in the measurements is observed at about 59 GHz (see Fig. 24). Despite this frequency shift, both the angular position and the overall extent of the gain drop are in good agreement with the simulated OSB behavior, confirming the theoretical expectations for a periodic LWA. The close match between simulation and measurement indicates that the observed effect is primarily governed by the antenna geometry rather than by fabrication imperfections or measurement artifacts. As a third measurement, the LWA fabricated with enlarged waveguide dimensions and metallized using a peristaltic pump was characterized. The measurement results show a significant improvement: the beam squint increased to the level predicted by simulation. The total squint angle now reaches 76° across both ports, in excellent agreement with the simulated performance. The realized gain also improved slightly and remains within the simulated range of 13–15 dB. As observed in previous configurations, a local gain drop near broadside is still present (see Fig. 25). To further assess

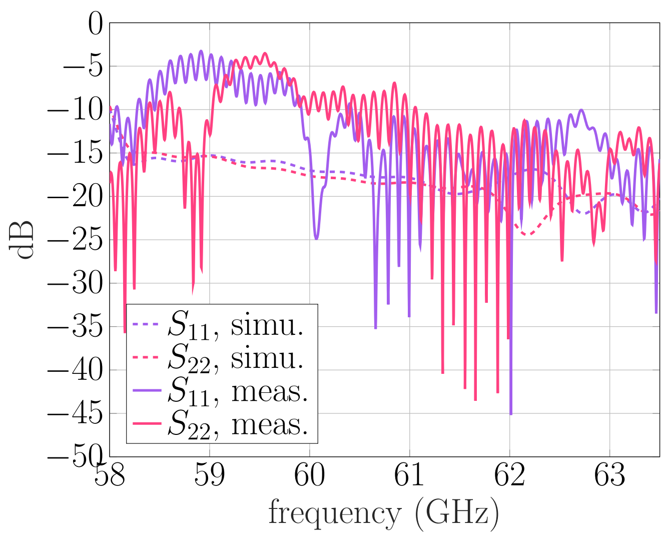

(a)

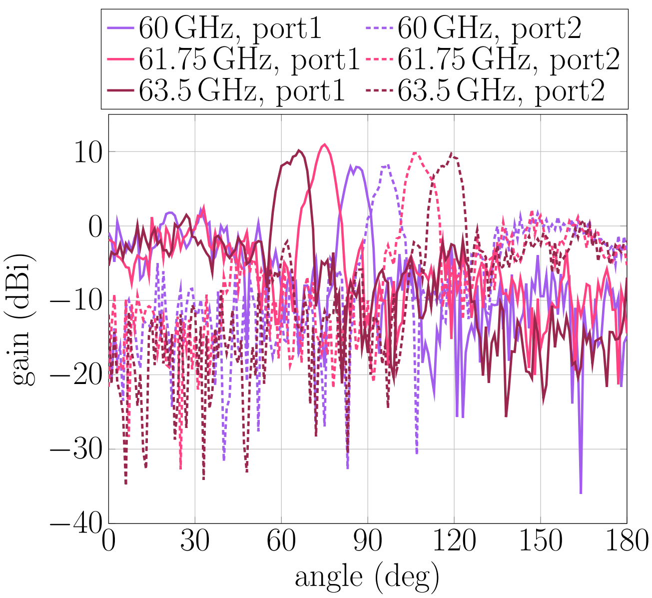

(b)

Fig. 24. Measurement results of the LWA metallized with a peristaltic pump. (a) Input reflection coefficients. (b) Far-field pattern using both ports.

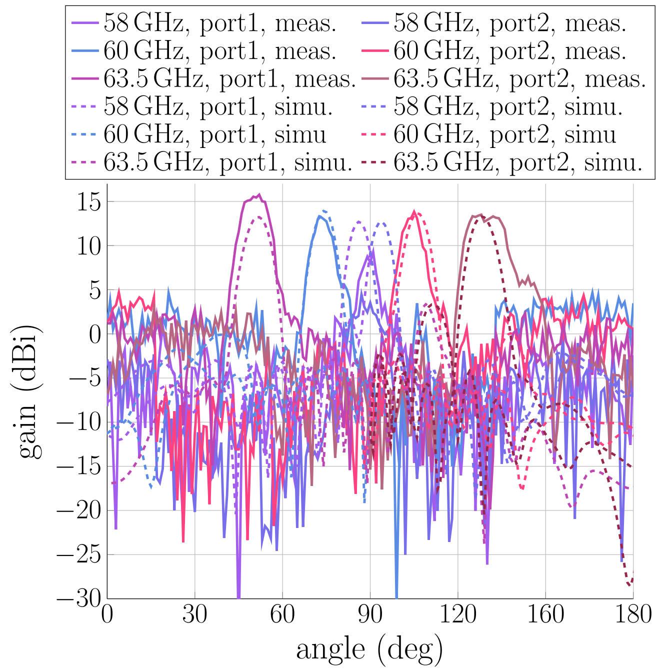

Fig. 25. Measurement and simulation results of the LWA with enlarged dimensions, metallized using a peristaltic pump.

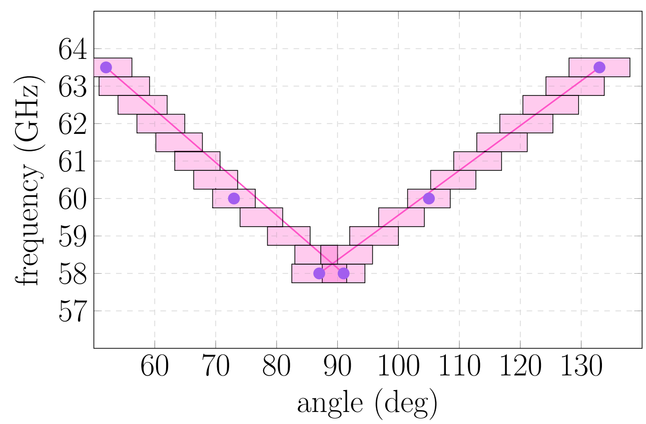

Fig. 26. Measured frequency–angle relationship of the serpentine LWA, showing the main beam trajectory and linear dispersion across the frequency range, closely matching the simulated behavior.

the performance of this improved antenna configuration, the measured radiation characteristics are compared in detail with the corresponding simulation results. In particular, the beam trajectories, beamwidths, and gain behavior over frequency are analyzed to evaluate the agreement between measurement and simulation and to quantify remaining deviations. The measured radiation patterns of the antenna closely follow the simulated results (see Fig. 25), with the main beams largely confined within the expected HBPW, as visualized by the pink boxes. Both the main-lobe trajectory and beamwidth show good agreement with the simulation. Slight deviations are observed at higher radiation angles, likely due to manufacturing tolerances or assembly effects. The measured linearity of the antenna in Fig. 26 confirms these trends, with the main beam angles of both ports covering the anticipated ranges and the dispersion remaining essentially linear. The quantitative analysis indicates a mean angular deviation of at most 1°–2° compared with the simulation, an rms gain error of approximately 1 dB (with slightly larger deviations only at broadside), and a frequency shift of the broadside gain of about 0.5 GHz. Overall, the measurements validate both the radiation characteristics and linearity of the antenna, with the observed discrepancies attributable to measurement and fabrication tolerances, demonstrating the suitability of the design for the intended application.

F. Angle Measurement

The last measurement aimed to demonstrate the principle of frequency-dependent angle determination with this antenna. For this purpose, as shown in Fig. 27(a) and (b), the LWA was placed on a rotating stage inside the measurement chamber,

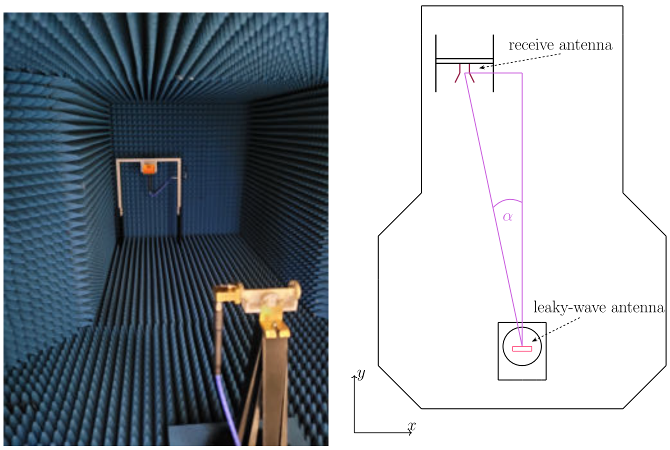

(a) (b)

Fig. 27. Setup for angle measurement with the LWA. (a) View inside the measurement chamber. (b) Sketch of the measurement setup.

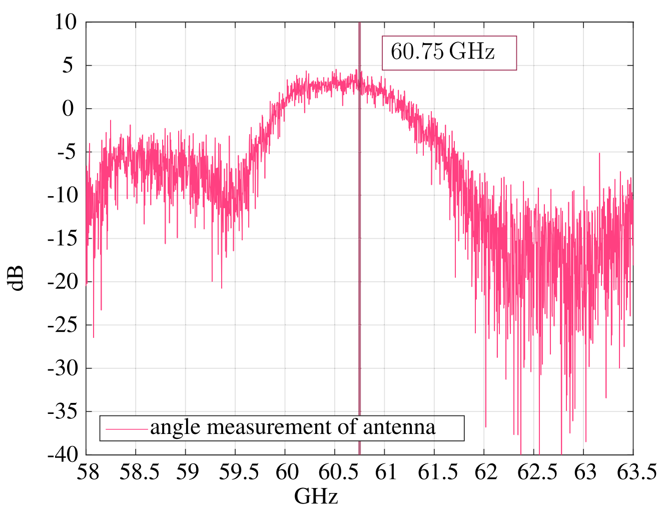

Fig. 28. Angle measurement with the LWA. Antenna gain over frequency.

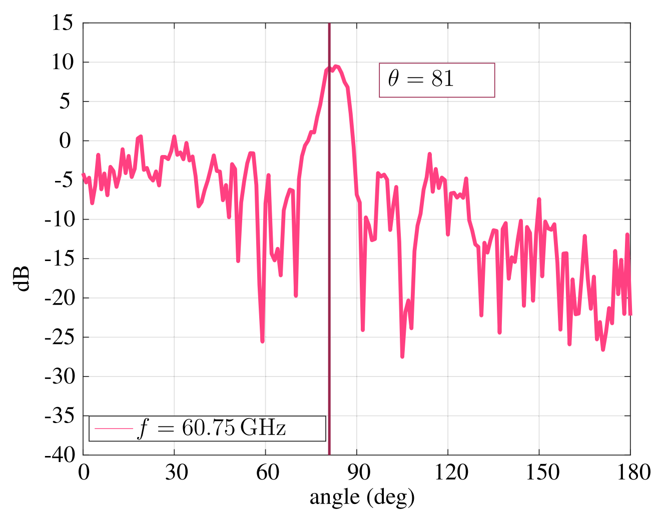

Fig. 29. Angle measurement with the LWA. Antenna gain over the azimuth angle.

with the slot plane perpendicular to the $\theta = 0°$ direction. The rotating stage served as a fixed mount, and no rotation occurred during measurement. Power was fed via Port 1 while systematically varying the frequency from 58 to 63.5 GHz. The measurement results (see Fig. 28) indicate that the maximum reception antenna gain occurred at approximately 60.75 GHz. The positioning of the receiving horn antenna by approximately 10° relative to the main beam direction leads to a reduction in antenna gain of about 4 dB, as expected from the known radiation pattern of the horn antenna. Consequently, the measured gain is approximately 5 dB lower than in the previous measurements. The remaining deviation of about 1 dB can be attributed to a suboptimal alignment between the transmitting and receiving antennas, including slight height and polarization mismatches. The far-field plot in Fig. 29 shows that the main beam direction is around $\theta = 81°$. Thus, the angle to be measured, $\alpha_{\text{measurement}}$, is determined as follows:

$$\alpha_{\text{measurement}} = 90° - 81° = 9°. \tag{24}$$

Since the target angle was set to 10°, the deviation is only 1°. These results confirm that the frequency-dependent beam steering principle of the LWA enables precise angle determination in an SISO radar system.

TABLE III
COMPARISON WITH LWAS FROM OTHER PUBLICATIONS

Publication	Squint Angle	rel. Bandwidth	Frequency Range
[18]	48°	34.3%	28 GHz - 40 GHz
[19]	7°	7.4%	91 GHz - 98 GHz
[20]	17°	18.8%	24 GHz - 29 GHz
[21]	19°	24.4%	9 GHz - 11.5 GHz
[22]	30.6°	37.5%	12 GHz - 18 GHz
[23]	39°	6%	9.7 GHz - 10.3 GHz
[10]	42°	16.6%	55 GHz - 65 GHz
this work	76°	9.1%	58 GHz - 63.5 GHz

G. Comparison

The published LWAs presented in Table III exhibit different characteristics in terms of frequency range, squint angle, and bandwidth. The antenna in [18] operates at a very high frequency of 95 GHz; however, the results presented are solely based on simulations. These simulations achieve a squint angle of 7° with a bandwidth of 7 GHz. The antennas from [19] and [20], and [21] operate at significantly lower frequency ranges between 9 and 29 GHz. While [19] and [20] achieve squint angles of 17° and 19°, respectively, the antenna in [21] demonstrates superior beam steering with 30.6°. However, it was fabricated using FDM metal printing, a technique that is impractical for 60 GHz due to excessive surface roughness at the slots and overall structure leading to significant losses for millimeter waves. A particularly notable antenna is the one presented in [22], which achieves a squint angle of 39° despite having a very narrow bandwidth of only 600 MHz. This highlights that a high squint angle can also be achieved with a narrow bandwidth. This antenna was also realized using a slightly different serpentine design. However, such a design would be difficult to implement at higher frequencies due to the tight structural tolerances required, which become increasingly challenging to maintain as the frequency increases. The antenna from [17] offers a large squint angle of 48° with a bandwidth of 12 GHz in the range of 28–40 GHz. This provides one of the best combinations of relative bandwidth and squint angle in the comparison but still operates well below the 60-GHz range.

In contrast to the previously published LWA based on a parallel-plate waveguide with a 10 GHz bandwidth and a squint angle of over 40° [2], the antenna presented in this work follows a new design approach. It uses a traveling-wave-fed slot structure, achieves a total scanning angle of 76° across a 5.5 GHz bandwidth, and prioritizes a robust, single-piece layout for improved manufacturability and reproducibility. The antenna is additively manufactured and silver-coated, ensuring a flexible and cost-efficient production process suitable for precise angle estimation in SISO radar systems. Overall, the comparison highlights the key challenges of high-frequency LWA design: manufacturing precision and the tradeoff between squint angle and bandwidth. While some existing designs achieve high squint angles, they often lack either a high operating frequency or a scalable manufacturing method. The presented antenna offers a unique combination of these properties, making this well-suited for compact and resource-limited 60 GHz SISO radar systems.

H. Conclusion and Outlook

In this work, a compact waveguide-based LWA was designed, additively manufactured, and experimentally characterized. The antenna employs a traveling-wave excitation of longitudinal slots and is realized as a mechanically robust, single-piece structure using high-resolution SLA 3-D printing. Beam steering of up to 76° was achieved over a reduced operational bandwidth of 5.5 GHz, enabled by a compact serpentine layout that enhances the frequency-dependent angular dispersion. Unlike prior works such as [10], the antenna is specifically optimized for enhanced angular resolution and large beam squint within a narrow frequency range, rather than for wideband coverage. The geometry was tailored to ensure electrical compatibility with Infineon's BGT60TR13 radar transceiver, facilitating integration into commercial SISO radar platforms. Experimental evaluation revealed that beam steering behavior is sensitive to both fabrication accuracy and surface metallization. Improvements in the additive manufacturing process, especially with respect to structural precision and uniformity of the silver coating, led to a significant reduction in unwanted scattering effects and angular deviations. Through the optimized 3-D-printing process and the refined metallization technique, the antenna performance is significantly enhanced, enabling for the first time a practical realization of this concept at millimeter-wave frequencies. While previous implementations have been practically validated only at lower frequencies, this work demonstrates the feasibility of precise and cost-efficient angular control even in the 60-GHz range. The presented results confirm that the proposed antenna provides a cost-efficient and scalable solution for resource-constrained radar applications. By leveraging additive manufacturing and design-driven angular control, the antenna combines low complexity with high directivity and is well-suited for integration into compact radar sensors requiring angular discrimination at minimal hardware effort.

References

[1] E. Fishler, A. Haimovich, R. Blum, D. Chizhik, L. Cimini, and R. Valenzuela, "MIMO radar: An idea whose time has come," in *Proc. IEEE Radar Conf.*, Philadelphia, PA, USA, Apr. 2004, pp. 71–78, doi: 10.1109/NRC.2004.1316398.

[2] J. Gabsteiger, T. Kurin, C. Dorn, A. Koelpin, and F. Lurz, "Antenna model and simulation platform for angle estimation with a SISO radar system," in *Proc. 21st Eur. Radar Conf. (EuRAD)*, Paris, France, Sep. 2024, pp. 192–195, doi: 10.23919/eurad61604.2024.10734874.

[3] M. Q. Nguyen, R. Feger, J. Bechter, M. Pichler-Scheder, M. H. Hahn, and A. Stelzer, "Fast-chirp FDMA MIMO radar system using range-division multiple-access and Doppler-division multiple-access," *IEEE Trans. Microw. Theory Techn.*, vol. 69, no. 1, pp. 1136–1148, Jan. 2021, doi: 10.1109/TMTT.2020.3039795.

[4] P. F. Sammartino, C. J. Baker, and H. D. Griffiths, "Frequency diverse MIMO techniques for radar," *IEEE Trans. Aerosp. Electron. Syst.*, vol. 49, no. 1, pp. 201–222, Jan. 2013, doi: 10.1109/TAES.2013.6404099.

[5] A. Hassanien, B. Himed, and B. D. Rigling, "A dual-function MIMO radar-communications system using frequency-hopping waveforms," in *Proc. IEEE Radar Conf. (RadarConf)*, May 2017, pp. 1721–1725, doi: 10.1109/RADAR.2017.7944485.

[6] W. Mayer, M. Wetzel, and W. Menzel, "A novel direct-imaging radar sensor with frequency scanned antenna," in *IEEE MTT-S Int. Microw. Symp. Dig.*, Jun. 2003, pp. 1941–1944.

[7] M. Skolnik, *Radar Handbook*, 2nd ed., New York, NY, USA: McGraw-Hill, 1990.

[8] K. Solbach and R. Schneider, "Antenna technology for millimeter wave automotive sensors," in *Proc. 29th Eur. Microwave Conf.*, 1999, pp. 139–142.

[9] J. Guan, S. Luo, and D. Li, "Blind deconvolution-based angular super-resolution algorithm for scanning radar system," in *Proc. CIE Int. Conf. Radar (RADAR)*, Guangzhou, China, Oct. 2016, pp. 1–4.

[10] J. Gabsteiger, D. Langer, C. Dorn, A. Koelpin, and F. Lurz, "60GHz leaky-wave antenna design for SISO radar systems with angle estimation," in *Proc. IEEE Radio Wireless Symp. (RWS)*, Jan. 2025, pp. 21–24, doi: 10.1109/RWS62086.2025.10904842.

[11] S. Alhuwaimel, "Fully polarimetric slotted waveguide antenna array," Ph.D. thesis, Univ. College London, London, U.K., 2018.

[12] C. A. Balanis, *Advanced Engineering Electromagnetics*. Hoboken, NJ, USA: Wiley, 2012.

[13] R. Elliott, *Antenna Theory and Design, Revised Edition*. Hoboken, NJ, USA: Wiley, 2003.

[14] R. Elliott, "An improved design procedure for small arrays of shunt slots," *IEEE Trans. Antennas Propag.*, vol. AP-31, no. 1, pp. 48–52, Jan. 1983.

[15] Á. Jaque Jiménez, G. Zamora, and J. Bonache, "Frequency-scanning leaky-wave slot antenna array based on serpentine waveguide with open stopband suppression," *IEEE Antennas Wireless Propag. Lett.*, vol. 23, pp. 344–348, 2024.

[16] H. Quan, T. Zhang, H. Xu, S. Luo, J. Nie, and X. Zhu, "Photo-curing 3D printing technique and its challenges," *Bioactive Mater.*, vol. 5, no. 1, pp. 110–115, Mar. 2020.

[17] Z. Liu, H. Lu, J. Liu, S. Yang, Y. Liu, and X. Lv, "Compact fully metallic millimeter-wave waveguide-fed periodic leaky-wave antenna based on corrugated parallel-plate waveguides," *IEEE Antennas Wireless Propag. Lett.*, vol. 19, no. 5, pp. 806–810, May 2020, doi: 10.1109/LAWP.2020.2980993.

[18] S. Singh and A. Basu, "Circularly polarized slotted waveguide leaky wave antenna at W band for radar application," in *Proc. Int. Symp. Antennas Propag. (ISAP)*, Oct. 2022, pp. 403–404, doi: 10.1109/ISAP53582.2022.9998854.

[19] M. Al Sharkawy and A. A. Kishk, "Long slots array antenna based on ridge gap waveguide technology," *IEEE Trans. Antennas Propag.*, vol. 62, no. 10, pp. 5399–5403, Oct. 2014, doi: 10.1109/TAP.2014.2345411.

[20] M. Vukomanovic, J.-L. Vazquez-Roy, O. Quevedo-Teruel, E. Rajo-Iglesias, and Z. Sipus, "Gap waveguide leaky-wave antenna," *IEEE Trans. Antennas Propag.*, vol. 64, no. 5, pp. 2055–2060, May 2016, doi: 10.1109/TAP.2016.2539376.

[21] K. Zhao, G. Senger, and N. Ghalichechian, "3D-printed frequency scanning slotted waveguide array with wide band power divider," in *Proc. United States Nat. Committee URSI Nat. Radio Sci. Meeting (USNC-URSI NRSM)*, Boulder, CO, USA, Jan. 2019, pp. 1–2, doi: 10.23919/USNC-URSI-NRSM.2019.8712999.

[22] W. Yin et al., "Frequency scanning single-ridge serpentine dual-slot-waveguide array antenna," *IEEE Access*, vol. 8, pp. 77245–77254, 2020.

Jasmin Gabsteiger (Student Member, IEEE) received the B.Sc. and M.Sc. degrees in electrical engineering from Friedrich-Alexander University Erlangen–Nuremberg (FAU), Erlangen, Germany, in 2019 and 2021, respectively, and the Dr.-Ing. degree from Otto von Guericke University Magdeburg, Magdeburg, Germany, in 2026.

From January 2022 to 2025, she was a Research Associate with the Institute for Electronics Engineering, FAU. Since 2026, she has been the Research Group Leader at Otto von Guericke University Magdeburg. Her research interests include radar systems, antenna design, and machine learning.

Dr. Gabsteiger is a member of the IEEE Microwave Theory and Techniques Society (MTT-S). She was a recipient of the IEEE Microwave Theory and Techniques Society Graduate Fellowship Award in 2024. In addition, she achieved the Second Place in the Student Design Competition at the IEEE International Microwave Symposium in 2022 and 2024. She won the first prize in the Best Paper Contest at the IEEE Radio and Wireless Week 2025.

Christian Robisch received the B.Sc. degree in electrical engineering from Friedrich-Alexander University Erlangen–Nuremberg (FAU), Erlangen, Germany, in 2025.

Mr. Robisch was a recipient of the "Semikron Danfoss Student Award" for outstanding academic performance in his bachelor's studies.

Alexander Koelpin (Fellow, IEEE) received the Diploma degree in electrical engineering and the Ph.D. and Habilitation degrees from Friedrich-Alexander University Erlangen–Nuremberg (FAU), Erlangen, Germany, in 2005, 2010, and 2014, respectively.

From 2005 to May 2017, he was with the Institute for Electronics Engineering, FAU. From 2007 to 2010, he was the Team Leader, from 2010 to 2015, he was the Group Leader of the Circuits, Systems, and Hardware Test Group, Erlangen, and since 2015, he has been the Leader of the Group Electronic Systems, Erlangen. From June 2017 to February 2020, he was a Professor and the Head of the Chair for Electronics and Sensor Systems, Brandenburg University of Technology Cottbus–Senftenberg, Cottbus, Germany. Since March 2020, he has been with Hamburg University of Technology, Hamburg, Germany, as a Professor and the Head of the Institute of High-Frequency Technology. He has authored or co-authored more than 300 publications in his areas of interest. His research interests are in the areas of microwave circuits and systems, radar and wireless sensing, wireless communication systems, local positioning, and six-port technology.

Dr. Koelpin was a member of the Commission A: Electromagnetic Metrology of U.R.S.I. from 2012 to 2017. He has been an Elected Member since 2018. He was awarded the IEEE MTT-S Outstanding Young Engineer Award in 2016 and the ITG Award of German VDE in 2017. He was the Chair of the IEEE MTT-S Technical Committee MTT-24, from 2018 to 2020. He has been the Vice Chair of the IEEE MTT-S/AP German Chapter Executive Board, since 2020. He was the Conference Co-Chair of the IEEE Topical Conference on Wireless Sensors and Sensor Networks, the Conference Chair of the 2020 German Microwave Conference, the Technical Program Chair of IEEE Radio and Wireless Week 2021, and the General Chair of IEEE Radio and Wireless Week 2023. He serves as a reviewer for several journals and conferences.

Fabian Lurz (Senior Member, IEEE) received the B.Sc. and M.Sc. degrees in information and communication technology and the Dr.-Ing. degree from Friedrich-Alexander University Erlangen–Nuremberg (FAU), Erlangen, Germany, in 2010, 2013, and 2019, respectively.

In 2013, he was a Research Assistant with the Institute for Electronics Engineering, FAU, and from 2017 to 2020, he was the Research Group Leader of the Circuits, Systems and Hardware Test Group. In June 2020, he was a Senior Engineer and the Research Group Leader with the Institute of High-Frequency Technology, Hamburg University of Technology, Hamburg, Germany. Since October 2023, he has been a Full Professor and the Head of the Chair of the Integrated Electronic Systems, Otto von Guericke University Magdeburg, Magdeburg, Germany. His research interests include microwave circuits and systems, especially for low-cost and low-power metrology applications.

Prof. Lurz is a member of the IEEE Microwave Theory and Techniques Society and the IEEE Instrumentation and Measurement Society. He was a recipient of the First Prize of the High Sensitivity Radar Student Design Competition of the IEEE International Microwave Symposium in 2014, 2017, and 2018, respectively, and the IEEE Microwave Theory and Techniques Society Graduate Fellowship Award in 2016.